

The *Fermi* blazars' divide based on the diagnostic of the SEDs peak frequencies

A. Tramacere^{*}, E. Cavazzuti[†], P. Giommi[†], N. Mazziotta^{**,‡} and C. Monte^{**,‡}

on behalf of the *Fermi*-LAT collaboration

^{*}*ISDC, Data Centre for Astrophysics, Chemin d'Ecogia 16, CH-1290 Versoix, Switzerland.*

e-mail: andrea.tramacere@unige.ch

[†]*Agenzia Spaziale Italiana (ASI) Science Data Center, I-00044 Frascati (Roma), Italy*

^{**}*Dipartimento di Fisica, "M.Merlin" dell' Università e del Politecnico di Bari, Italy*

[‡]*Istituto Nazionale di Fisica Nucleare, Sezione di Bari, 70126 Bari, Italy*

Abstract. We have studied the quasi-simultaneous Spectral Energy Distributions (SED) of 48 LBAS blazars, detected within the three months of the LAT Bright AGN Sample (LBAS) data taking period, combining *Fermi* and *Swift* data with radio NIR-Optical and hard- X/gamma-ray data.

Using these quasi-simultaneous SEDs, sampling both the low and the high energy peak of the blazars broad band emission, we were able to apply a diagnostic tool based on the estimate of the peak frequencies of the synchrotron (S) and Inverse Compton (IC) components.

Our analysis shows a *Fermi* blazar's divide based on the peak frequencies of the SED. The robust result is that the Synchrotron Self Compton (SSC) region divides in two the $\nu_p^S - \gamma_p^{SSC}$ plane. Objects within or below this region, radiating likely via the SSC process, are high-frequency-peaked BL Lac object (HBL), or low/intermediate-frequency-peaked BL Lac object (LBL/IBL). All of the IBLs/LBLs within or below the SSC region are not Compton dominated.

The objects lying above the SSC region, radiating likely via the External radiation Compton (ERC) process, are Flat Spectrum Radio Quasars and IBLs/LBLs. All of the IBLs/LBLs in the ERC region show a significant Compton dominance.

Keywords: Active and peculiar galaxies and related systems (including BL Lacertae objects, blazars, Seyfert galaxies, Markarian galaxies, and active galactic nuclei), Gamma rays astronomical observations,

PACS: 98.54.Cm, 95.85.Pw

1. INTRODUCTION

Blazars objects are Active Galactic Nuclei (AGNs) characterized by a polarised and highly variable non-thermal continuum emission extending from radio to γ -rays. In the most accepted scenario, this radiation is produced within a relativistic jet that originates in the central engine and points close to our line of sight. Since the relativistic outflow moves with a bulk Lorentz factor (Γ) and is observed at small angles ($\theta \simeq 1/\Gamma$), the emitted fluxes are affected by a beaming factor $\delta = 1/(\Gamma(1 - \beta \cos \theta))$.

Despite these objects have been observed for more than 40 years over the entire electromagnetic spectrum, still present puzzling behaviours. Indeed, their complex multi-wavelength variability requires the use of simultaneous multi-frequency data to fully

understand the underlying physical scenario.

The study of the Spectral Energy Distribution (SED) of blazars has been largely enriched since July 2008 after the beginning of the scientific activity of the γ -ray Large Area Telescope (LAT) [1] on board *Fermi*-GST [2].

A detailed investigation of the broad-band spectral properties of 48 γ -ray selected blazars observed by *Fermi* is reported in [3]. The quasi-simultaneous SEDs presented in that paper were obtained using data from *Fermi* operating in survey mode, combined to simultaneous data from *Swift*, and other high-energy astrophysics satellites mission on orbit, complemented by other space and ground-based observatories.

Here we focus on the physical implications of these SEDs, using the peak frequencies of the synchrotron (S) and inverse Compton (IC) component as a diagnostic tool to discriminate among different emission scenarios.

2. IMPLICATIONS FOR PHYSICAL MODELING

The quasi-simultaneous SEDs reported in [3, 4, 5] show the typical two bump shape that is seen in radio or X-ray selected blazars. According to current models the low energy bump is interpreted as synchrotron emission from highly relativistic electrons, and the high energy bump is related to inverse Compton emission of various underlying radiation fields.

In the case of synchrotron self Compton model (SSC) [6, 7] the seed photons for the IC process are the synchrotron photons produced by the same population of relativistic electrons.

In the case of external radiation Compton (ERC) scenario [8, 9], the seed photons for the IC process are typically UV photons generated by the accretion disk surrounding the black hole, and reflected toward the jet by the Broad Line Region (BLR) within a typical distance from the accretion disk of the order of one pc. If the emission occurs at larger distances, the external radiation is likely to be provided by a dusty torus (DT) [10]. In this case the photon field is typically peaked at IR frequencies.

Blazars come in two main flavours: BL Lac objects and Flat Spectrum Radio Quasars (FSRQ). The former type is characterised by featureless optical spectra and their SEDs are usually interpreted in the framework of pure SSC scenario. On the contrary, FSRQs display the prominent emission lines that are typical of QSOs, and are likely to have the IC component dominated by the ERC emission. BL Lac objects are often subdivided into three subclasses depending on their SEDs. This classification [11] uses the peak energy of the synchrotron emission, which reflects the maximum energy the particles can be accelerated in the jet, to classify BL Lacs into low energy, intermediate energy and high energy synchrotron peak objects, respectively called LBL, IBL and HBL.

We follow a phenomenological approach to obtain information about the peak Lorentz factor of the electron distribution (γ_p) most contributing to the synchrotron emission and to the inverse Compton process. To test the methods used to estimate γ_p , we employ an accurate numerical model [12, 13, 14, 15] that can reproduce both the SSC and ERC models. For the electron distribution we considered a log-parabola of the form

$n(\gamma) = K \cdot 10^r \text{Log}(\gamma/\gamma_p)^2$ with γ_p ranging between 100 and $6 \cdot 10^5$ and with curvature parameter $r = 2.0$ [16, 17]. As input parameter for the benchmark SSC model we use a source size $R = 10^{15}$ cm, a magnetic field $B = 0.1$ G, a beaming factor $\delta = 10$, and an electron density $N=1 \text{ e}^-/\text{cm}^3$ ($N=\int n(\gamma)d\gamma$). In the case of the benchmark ERC model, we use the same set of parameters with the addition of the external photon field produced by the accretion disk and reflected by the BLR toward the emitting region with an efficiency $\tau_{BLR} = 0.1$. The accretion disk radiation is modelled by a multitemperature black body, with a innermost disk temperature of 10^5 K.

3. THE SYNCHROTRON PEAK FREQUENCY

The dependence of the observed peak frequency of the synchrotron emission (ν_p^S) on magnetic field intensity (B), electron Lorentz factor (γ), beaming factor (δ) and redshift (z) is given by:

$$\nu_p^S = 3.2 \times 10^6 (\gamma_p^S)^2 B \delta / (1+z) = \nu_p^{S'} \delta / (1+z). \quad (1)$$

where $\nu_p^{S'}$ is the synchrotron peak frequency in the emitting region rest-frame. A good estimate of γ_p^S in terms of the differential electron energy distribution ($n(\gamma) = dN(\gamma)/d\gamma$) is given by the peak of $\gamma^3 n(\gamma)$, hereafter γ_{3p} [12, 17]. The value of γ_p^S is estimated by fitting the peak of the numerically computed synchrotron SED with a log-parabolic analytical function. Note, however, that there is a degeneracy on the value of γ_p^S given by the product $B\delta$. We discuss this point in the next sections.

4. THE INVERSE COMPTON PEAK FREQUENCY

In a simple SSC model, and under the Thomson regime (TH) of the IC scattering, the observed peak frequency of the synchrotron component (ν_p^S) is related to the observed peak frequency of the inverse Compton one (ν_p^{IC}) by the following relation:

$$\frac{\nu_p^{IC}}{\nu_p^S} \simeq \frac{4}{3} (\gamma_p^{SSC})^2 \quad (2)$$

where γ_p^{SSC} is of the same order of γ_p^S and of γ_{3p} . In the left panel of of Fig. 1 we plot the S and IC component for a SSC scenario for the choice of SSC parameters reported in Sect. 2. In the right panels (*a* and *b*) of the same figure we show that trend predicted by Eq. 2 is valid only for $\gamma_p^{SSC} \lesssim 2 \cdot 10^4$ where the transition from Thomson to Klein Nishina (KN) regime occurs. In the KN regime Eq. (2) is no longer valid: in fact, the kinematic limit for the maximum energy of the up-scattered photons in the emitting region rest-frame is:

$$\nu_{max}^{IC} = \frac{4\gamma^2 \nu_S}{1 + 4\gamma^2 (h\nu_S/m_e c^2)}. \quad (3)$$

As the energy of the seed photons in the electron rest-frames increases, the maximum up-scattered photon energies approaches the energy of the up-scattering electron

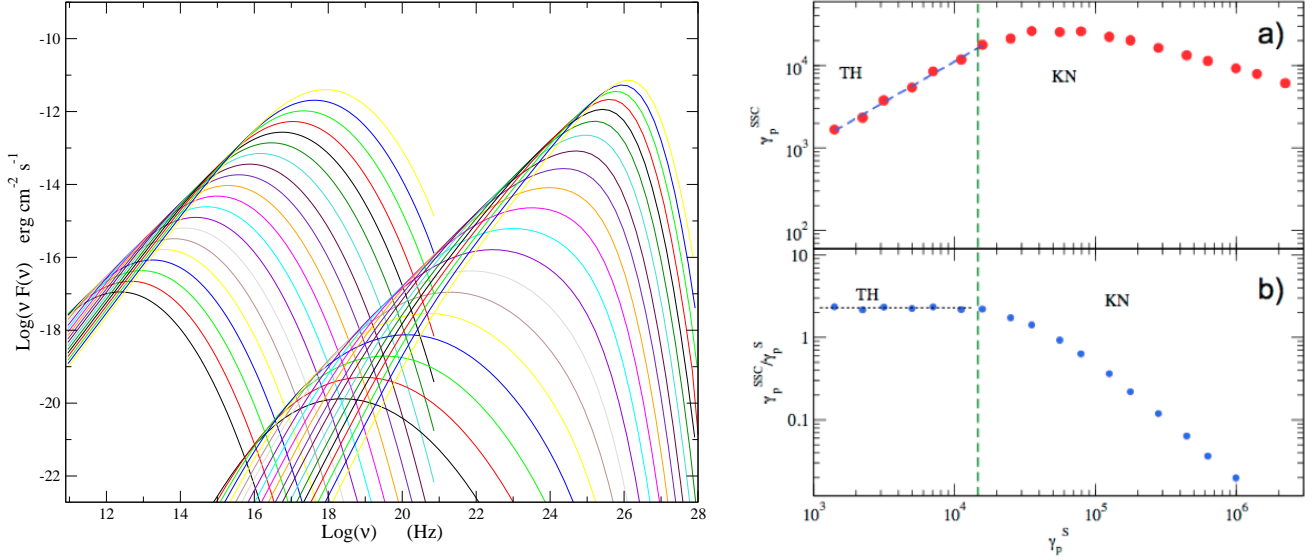


FIGURE 1. *Left panel:* SSC SEDs obtained using as electron distribution a log-parabola $n(\gamma) = K \cdot 10^r \text{Log}(\gamma/\gamma_p)^2$ with γ_p ranging between 100 and $6 \cdot 10^5$, and the curvature parameter $r = 2.0$. The other model parameters are: source size $R = 10^{15}$ cm, a magnetic field $B = 0.1$ G, a beaming factor $\delta = 10$, and an electron density $N = 1 \text{ e}^-/\text{cm}^3$ ($N = \int n(\gamma) d\gamma$). *Right panels:* Estimate of γ_p^S and γ_p^{SSC} for numerically computed SEDs showed in the left panel. From top to bottom: *a)* γ_p^{SSC} as a function of γ_p^S , the transition from the TH trend (blue dashed line) to the KN region is evident for $\gamma > 2 \cdot 10^4$. *b)* The ratio of γ_p^{SSC} to γ_p^S , also in this case, above the TH region (vertical dashed green line) it is evident the effect of the KN suppression, γ_p^{SSC} gets to increasingly underestimate γ_p^S as γ_p^S is increasing.

($\gamma m_e c^2$). This means that the peak energy of the IC emission is no longer growing with $(\gamma_p^{SSC})^2$ according to Eq. (2), but it starts becoming smaller as shown in panels *a* and *b* of Fig. 1. Above the TH region (vertical dashed green line), it is evident the effect of the KN suppression, and γ_p^{SSC} gets to increasingly underestimate γ_p^S as γ_p^S is increasing. We note that this effect is particularly relevant for the case of HBL objects.

Other deviations from the trend predicted by Eq. (2) occur when further radiative components add to a single zone SSC. In fact, for the case of External Compton scenario, the observed peak frequency of the ERC component in terms of the frequency of the external photon field in the disk rest-frame ($\nu_p'^{EXT}$) reads:

$$\frac{\nu_p^{ERC}}{\nu_p'^{EXT}\Gamma} \simeq \left(\frac{4}{3}\right) (\gamma_p^{ERC})^2 \delta / (1+z) \quad (4)$$

where $\nu_p'^{EXT}\Gamma$ is the external photon field frequency transformed to the rest-frame of the emitting region which is moving with a bulk Lorentz factor Γ , and assuming that the BLR radiation is isotropic.

If one uses Eq. (2) in place of Eq. (4) (an assumption justified by the fact that the UV and IR external radiation fields are usually dominated by the non-thermal synchrotron

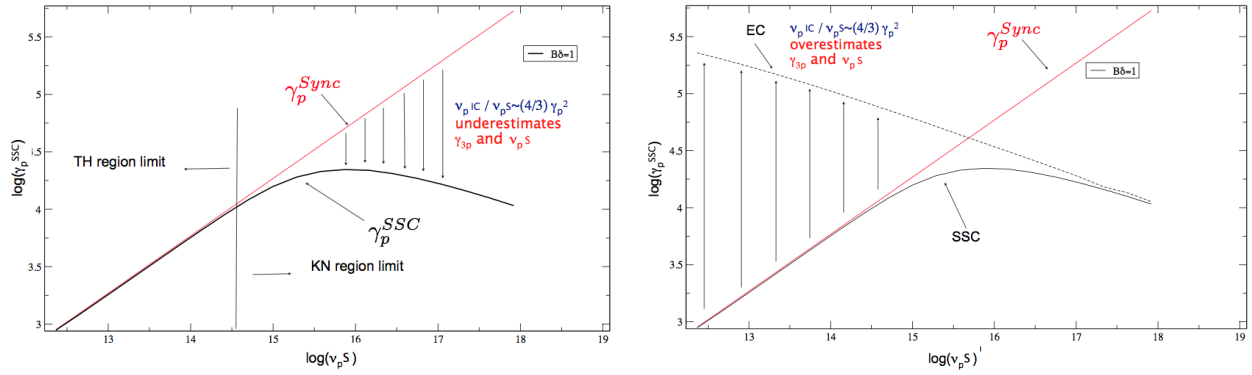


FIGURE 2. *Left Panel:* graphical representation of the deviation from the trend in Eq. 2 in the case of SSC emission in KN regime. *Right panel:* graphical representation of the deviation from the trend in Eq. 2 in the case of ERC emission.

emission of the source), a significant bias on the value of γ_p^{ERC} is introduced. In fact, the resulting value of γ_p is strongly overestimated in the case of external UV radiation field ($\gamma_p^{SSC} \gg \gamma_p^{ERC}$ and $\gamma_p^{SSC} \gg \gamma_p^S$). In the case of IR external radiation field, the bias is smaller but the measured value of γ_p^{SSC} is still overestimating both γ_p^{ERC} and γ_p^S .

In conclusion, when γ_p is estimated through Eq. (2) we expect two main biases:

1. a bias related to the KN effect, affecting mostly objects radiating via SSC under the KN regime, which leads to an underestimate of γ_p^S and γ_{3p} . This trend is reported in the left panel of Fig. 2.
2. A bias related to the ERC scenario, which yields an overestimate of γ_p^S and γ_{3p} . This trend is reported in the right panel of Fig. 2.

5. APPLICATION OF THE PEAK DIAGNOSTIC TOOL TO THE LBAS MW SEDS

The arguments presented in the previous section provide an interesting diagnostic tool in the $v_p^S - \gamma_p^{SSC}$ plane. Since under the TH regime $\gamma_p^S \simeq \gamma_p^{SSC}$, we expect objects radiating γ -rays mainly via the SSC/TH mechanism to lay along the $\gamma_p^S \propto v_p^S$ line, and below it in the case of SSC/KN regime. Objects radiating mainly via the ERC mechanism are expected to lay above the $\gamma_p^S \propto v_p^S$ line. A schematic expectation for this divide is plotted in Fig. 3, where the dashed black line represents the $\gamma_p^S \propto v_p^S$ trend, the solid blue line represents the SSC trend from the TH to the KN regime, and the dashed purple line represents the ERC trend.

As a caveat, we remind the reader that the peak frequencies derived in [3] may have systematics. Indeed, for sources peaking below (MeV blazars or LBL) or above (HBLs) the *Fermi* window, the peak frequency extrapolated from the polynomial fit [see 3, 5, 4], may have an uncertainty up to a factor of two. A more detailed analysis that takes this

effect into account will be presented in a further paper. We stress that this bias can affect only these single sources and the understanding of some outliers, and does not affect the overall trend that is the goal of the present analysis.

To test this scenario we use the values of γ_{peak}^{SSC} obtained by Eq. (2) applied to the numerically computed SSC/ERC SEDs, and we compare these trends with those obtained applying Eq. (2) to the observed peak frequencies and fluxes reported in the Tab. 13 of [3].

Fig. 4 shows the location of HBL objects (blue solid boxes), IBLs/LBLs objects (orange solid boxes) and FSRQs (red solid circles).

The values of γ_{peak}^{SSC} estimated for the case of SSC emission (dashed blue line with stars) show clearly the effect of the transition from the TH to the KN regime. We note that all but two of the HBLs lay below the $\gamma_p^S \propto \nu_p^S$ line. In particular all the HBL objects below the $\gamma_p^S \propto \nu_p^S$ line have γ_p^{SSC} values below the prediction of the SSC scenario (solid blue line), confirming, as expected, that the SSC emission occurs under the KN regime.

On the contrary, all the FSRQs and the LBL/IBL objects but one lay above the $\gamma_p^S \propto \nu_p^S$ line. All the FSRQs objects but one have a value of γ_p^{SSC} in excess of a factor $\sim 10^4$ and limited by the prediction from the ERC model (purple dashed line with stars). The LBLs/IBLs sources are more uniformly distributed across the region delimited by the the SSC TH prediction and by the ERC one.

By further dividing the sample in Compton Dominated (CD) objects ($S_p^{IC} > 2 S_p^S$)¹ and non-Compton Dominated (NCD) objects ($S_p^{IC} \leq 2 S_p^S$), we found that all the CD objects lay above the $\gamma_p^S \propto \nu_p^S$ line and populate the region between the SSC TH and the ERC regime, with the FSRQs clustering toward the ERC region.

Our analysis shows that the ERC model could explain the high CD values as well as the high values of γ_p^{SSC} estimated in the case of FSRQs and IBLs/LBLs. In order to explain the high values of γ_p^{SSC} obtained in the case of FSRQs in the context of single zone SSC emission model, a very small value of the magnetic field with ($B < 0.01$ G) is required.

5.1. $B\delta$ degeneracy and Monte Carlo approach

As a final step, we discuss two additional effects that have consequences for the source distribution in this parameter space:

1. The $B\delta$ degeneracy on γ_p^S can affect the transition region from TH to KN regime, since high values of δ allow the TH regime to propagate towards higher frequencies.

¹ We indicate $\nu_p F(\nu_p)$ as S_p

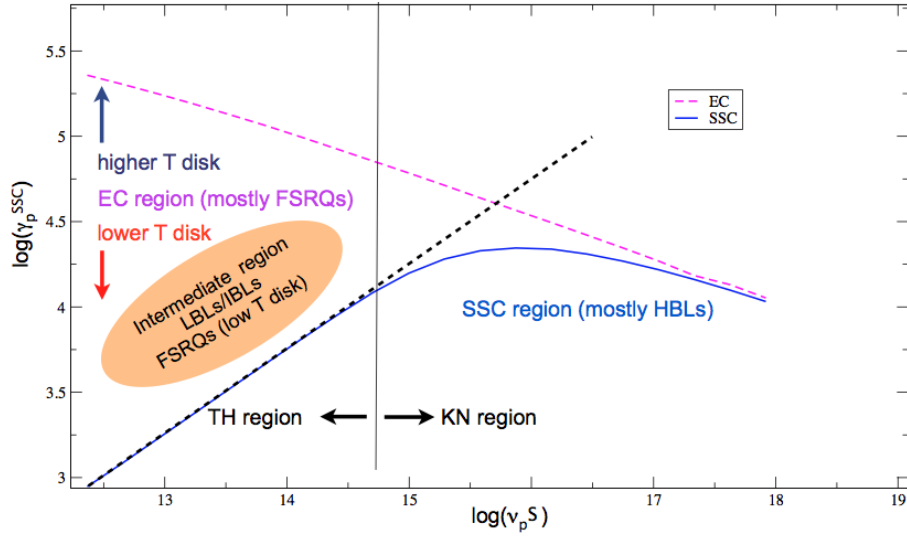


FIGURE 3. Schematic representation of the divide predicted by the SSC/KN and ERC deviations from the Eq. 2 trend. The dashed black line represent the $\gamma_p^S \propto \nu_p^S$ trend, the solid blue line represents the SSC trend from the TH to the KN regime, and the dashed purple line represents the ERC trend.

2. The values of γ_p in the case of an UV external radiation field (purple line Fig.4) constitutes an upper limit to the observed values of γ_p , meaning that objects in the region below the ERC prediction line require a wider range of external photon energies, extending down to the IR band.

To take into account both these effects we perform Monte Carlo (MC) simulations. Specifically, we generate both the SSC and ERC numerical computation of the SEDs extracting δ , B and the temperature of the accretion disk T from a random uniform distribution, in order to cover a larger volume of the parameter space. We generate 1000 realizations, with δ ranging in the interval [10-15], B in the interval [0.01-1] G and T in the interval [10 – 10^{4.5}] K. In Fig. 4 the MC results for the case of SSC lay within the area delimited by the blue contour line, while the results in the case of ERC model, are delimited by the light red contour line.

When we compare the observed data with the MC results, we note the following:

1. The MC simulations, compared to the ERC one for the only case of UV external photons (purple line), cover a much wider region of the parameter space. In the case of the MC SEDs, the range of temperatures of the BB emission allows us to take into account external photon fields peaking at IR frequencies. The FSRQs and IBLs/LBLs populate the whole parameter space delimited by the ERC/UV (purple line) and the SSC/TH case (solid blue line, below about 10¹⁵ Hz). This suggests, that in the ERC paradigm, the observed data concerning FSRQs (red circles) and IBLs/LBLs (orange square symbols), require external photon fields ranging from the UV down to the IR.

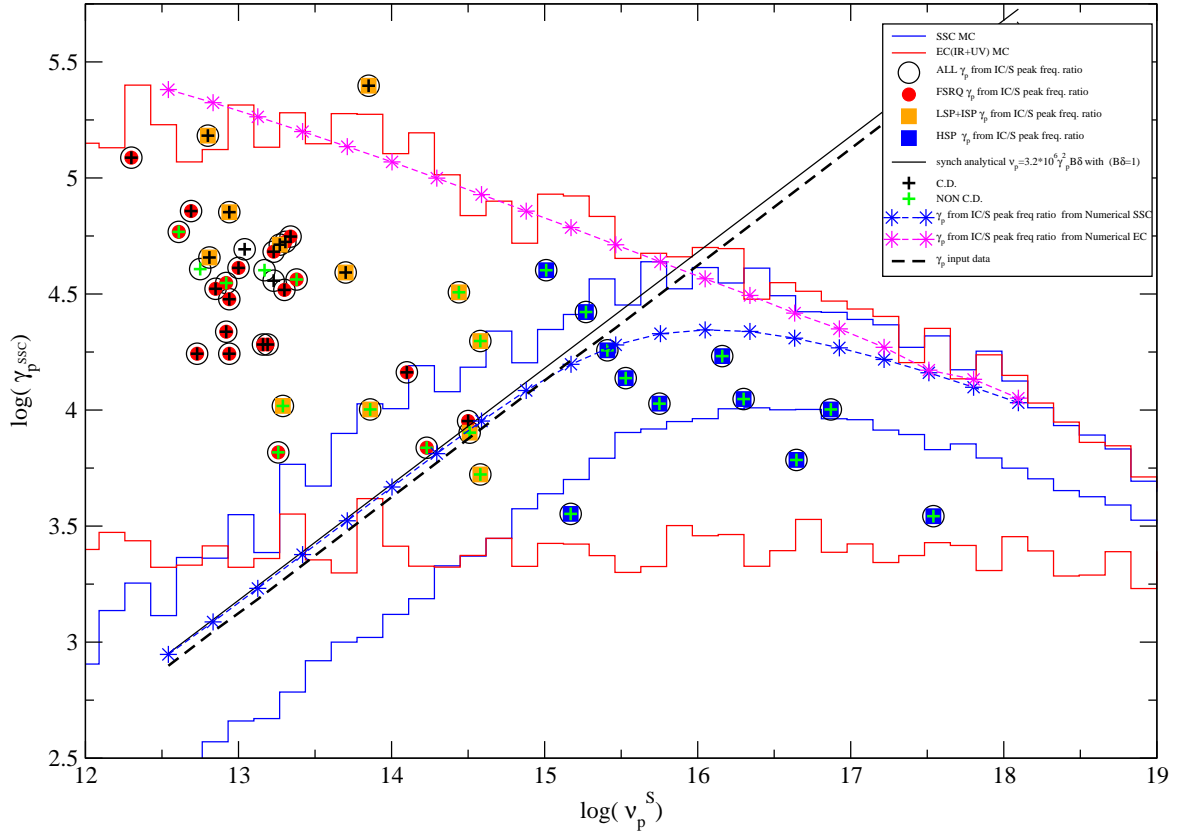


FIGURE 4. γ_p^{SSC} obtained by Eq. 2 for the objects reported in Table 10. blue solid boxes represent HPB objects, orange solid boxes represent IPBs/LPBs objects and red solid circles represent FSRQs. The black solid line represents ν_p^S estimated by Eq. (1) for both the ERC and the SSC numerical SEDs, the blue solid line represents γ_p^{SSC} estimated from Eq. (2) applied to numerically computed the SSC SEDs, and the solid purple line represents the same for the case of ERC emission. The true value of the simulation is represented by the black dashed line. Parameters of the model are given in Sect. 9. The blue and red contours delimit the area covered by the estimate of γ_p^{SSC} for the case of SSC and ERC models respectively and for a Monte Carlo simulation with values of δ ranging between 10 and 15, B ranging between 0.01 and 1G and T ranging between 10 and $10^{4.5}$ K.

2. In the case of the MC realization, all the HBLs and all the non-Compton dominated LBLs/IBLs are compatible with the SSC prediction, both in TH and KN regime.
3. All the FSRQs but four, are not compatible with the MC SSC region. Two of the FSRQs consistent with the MC SSC region, are non-CD.
4. All the LBLs/IBLs that are CD, are not consistent with the MC SSC.
5. the empty circles in Fig. 4, are blazars of unknown type.

6. DISCUSSION AND CONCLUSIONS

Trough the construction of quasi-simultaneous SEDs, sampling both the low and the high energy peak of the blazars broad band emission, we were able to apply a diagnostic tool based on the ratio of the peak frequencies. We studied the deviations from the trend predicted by Eq. 2, given by the KN regime (relevant to the case of HBLs), and by the ERC emission (relevant to the case of FSRQs), we were able to discriminate among different emission scenarios.

Our analysis shows that the HBL objects attend the SSC prediction, and that the values of γ_p^{SSC} returned for sources peaking above about 10^{15} Hz are within the KN limit expectation. All of the HBLs are not CD, as expected in the case of SSC emission. FSRQs populate mainly the ERC region of Fig. 4, and the dispersion on the values of γ_p^{SSC} hints for a dispersion in the typical temperature of the BB emission. This dispersion on the temperature is consistent with the dominant external photon field originating from some sources in the BLR, and in the DT for others.

All of the FSRQs but 5, are Compton Dominated. Two of the non-CD FSRQs lay close the SSC/TH region.

The LBL/IBL objects cover the region of Fig. 4 ranging from the SSC/TH to the ERC/BLR. The non-CD LBLs/IBLs are consistent with the SSC/TH region. On the contrary, the CD LBLs/IBLs cluster in the ERC/BLR region. This feature is very interesting since many BL Lac objects, and BL Lacertae itself, show intermittent emission lines. At this regard a monitoring of the optical spectrum compared the γ -rayflaring state and Compton dominance could be very useful to confirm the ERC component also for this class of objects.

In conclusion, our analysis shows a *Fermi* blazar's divide, based on the peak frequencies of the SED. The robust result is that the SSC region divides in two the ν_p^S – γ_p^{SSC} plane. Objects within or below this region, radiating likely via the SSC process are HBLs, and IBLs/LBLs without Compton dominance.

The objects lying above the SSC region, radiating likely via the ECR process, are FSRQs and IBLs/LBLs and are mostly Compton dominated.

ACKNOWLEDGMENTS

The *Fermi* LAT Collaboration acknowledges the generous support of a number of agencies and institutes that have supported the *Fermi* LAT Collaboration. These include the National Aeronautics and Space Administration and the Department of Energy in the United States, the Commissariat à l’Energie Atomique and the Centre National de la Recherche Scientifique / Institut National de Physique Nucléaire et de Physique des Particules in France, the Agenzia Spaziale Italiana and the Istituto Nazionale di Fisica Nucleare in Italy, the Ministry of Education, Culture, Sports, Science and Technology (MEXT), High Energy Accelerator Research Organization (KEK) and Japan Aerospace Exploration Agency (JAXA) in Japan, and the K. A. Wallenberg Foundation, the Swedish Research Council and the Swedish National Space Board in Sweden.

Additional support for science analysis during the operations phase from the following agencies is also gratefully acknowledged: the Istituto Nazionale di Astrofisica in Italy and the K. A. Wallenberg Foundation in Sweden. This research is based also on observations with the 100-m telescope of the MPIfR (Max-Planck-Institut für Radioastronomie) at Effelsberg.

REFERENCES

1. Atwood W. B. et al., *The Astrophysical Journal* **697**, 1071–1102 (2009), URL <http://adsabs.harvard.edu/abs/2009ApJ...697.1071A>, 0902.1089.
2. S. Ritz, *Overview of the GLAST Mission and Opportunities*, vol. 921, AIP, 2007, URL <http://link.aip.org/link/APCPCS/v921/i1/p3/s1\&Agg=doi>.
3. Abdo A. A. et al., *ArXiv e-prints* (2009), 0912.2040.
4. Monte, C., *These proceedings* (2010).
5. Gasparrini, D., *These proceedings* (2010).
6. T. W. Jones, S. L. O'dell, and W. A. Stein, *The Astrophysical Journal* **188**, 353 (1974), ISSN 0004-637X, URL <http://adsabs.harvard.edu/doi/10.1086/152724>.
7. G. Ghisellini, and L. Maraschi, *The Astrophysical Journal* **340**, 181 (1989), ISSN 0004-637X, URL <http://adsabs.harvard.edu/doi/10.1086/167383>.
8. M. Sikora, M. C. Begelman, and M. J. Rees, *The Astrophysical Journal* **421**, 153 (1994), ISSN 0004-637X, URL <http://adsabs.harvard.edu/doi/10.1086/173633>.
9. C. D. Dermer, and R. Schlickeiser, *The Astrophysical Journal* **575**, 667–686 (2002), ISSN 0004-637X, URL <http://stacks.iop.org/0004-637X/575/i=2/a=667>.
10. M. Sikora, M. Blazejowski, R. Moderski, and G. M. Madejski, *The Astrophysical Journal* **577**, 78–84 (2002), ISSN 0004-637X, URL <http://stacks.iop.org/0004-637X/577/i=1/a=78>.
11. P. Padovani, and P. Giommi, *Monthly Notices of the Royal Astronomical Society* **277**, 1477–+ (1995), arXiv:astro-ph/9511065.
12. A. Tramacere, P. Giommi, M. Perri, F. Verrecchia, and G. Tosti, *Astronomy and Astrophysics* **501**, 879–898 (2009), ISSN 0004-6361, URL <http://www.aanda.org/10.1051/0004-6361/200810865>.
13. A. Tramacere, *Spectral Variability in Blazar's High Energy Emission*, Ph.D. thesis, La Sapienza University, Rome (2007).
14. E. Massaro, A. Tramacere, M. Perri, P. Giommi, and G. Tosti, *Astronomy and Astrophysics* **871**, 861–871 (2006).
15. A. Tramacere, and G. Tosti, *New Astronomy Review* **47**, 697–699 (2003), arXiv:astro-ph/0306315.
16. E. Massaro, M. Perri, P. Giommi, and R. Nesci, *Astronomy and Astrophysics* **413**, 489–503 (2004), ISSN 0004-6361, URL <http://www.edpsciences.org/10.1051/0004-6361:20031558>.
17. A. Tramacere, F. Massaro, and A. Cavaliere, *Astronomy and Astrophysics* **466**, 521–529 (2007), arXiv:astro-ph/0702151.